The Astrophysical Journal, 653:425–436, 2006 December 10

PROPERTIES AND FORMATION OF THE MULTIPLE PROTOSTELLAR SYSTEM L1551 IRS 5

Jeremy Lim
Institute of Astronomy and Astrophysics, Academia Sinica, P.O. Box 23-141, Taipei 106, Taiwan; jlim@asiaa.sinica.edu.tw

and

Shigehisa Takakuwa
National Astronomical Observatory of Japan, ALMA Project Office, Osawa 2-21-1,
Mitaka, Tokyo 181-8588, Japan; s.takakuwa@nao.ac.jp
Received 2006 July 10; accepted 2006 August 14

ABSTRACT

We present an observation of L1551 IRS 5 at 7 mm with an angular resolution as high as $\sim 0\farcs04$ (5 AU). Apart from the two main components oriented north-south with a projected separation of 47 AU, we discover a third component lying 13 AU to the southeast of the northern component, thereby making L1551 IRS 5 a triple protostellar system. The two main components comprise circumstellar dust disks with dimensions of $\sim$17 AU, together with bipolar ionized jets collimated within a radial distance of $\lesssim$3 AU from their central protostars. The third component likely has an even smaller circumstellar dust disk with a dimension of $\sim$9 AU. The relative proper motion of the two main components is consistent with a circular coplanar orbit with an orbital separation of $\sim$50 AU, orbital period of $\sim$380 yr, and total mass of $\sim 0.9\ M_{\odot}$. Their measured disk sizes are smaller than the predicted gravitationally truncated sizes of $\sim$26 AU. Together with the predicted minimum size for a circumbinary gap, noncircular coplanar orbits are constrained to an eccentricity $\lesssim 0.3$. The disks of the two main components are accurately aligned with each other, as well as with a surrounding molecular pseudodisk. Furthermore, the clockwise orbital motion of these components coincides with the clockwise rotational motion of the pseudodisk. These attributes constitute a smoking gun for the formation of the two main components as a result of fragmentation within the inner regions of their parent pseudodisk. By contrast, the disk of the third component is significantly misaligned; measurements of its relative proper motion are required in order to help deduce its origin.

Subject headings: binaries: close — circumstellar matter — stars: formation — stars: individual (L1551 IRS 5) — stars: low-mass, brown dwarfs

Online material: color figures

1. INTRODUCTION

Our current understanding of star formation is based primarily on a framework for the formation of single stars such as the Sun (Shu et al. 1987). Yet, the vast majority of stars actually form as members of binary or multiple systems (Duquennoy & Mayor 1991; Mathieu 1994; Duchêne et al. 2006). As the frequency of multiplicity among low-mass stars at the pre-main sequence may be even higher than that at the main sequence, the formation of (most) multiple star systems is thought to occur during the protostellar phase.

There are a number of competing theoretical models for how multiple protostellar systems form, the leading candidates of which are, currently, fragmentation and capture (e.g., see the review by Tohline 2002). These models make simple but different predictions for the properties of the resulting protostellar systems. For example, fragmentation of a disklike condensation of molecular gas and dust (i.e., pseudodisk; Galli & Shu 1993) is expected to produce systems with circumstellar disks that are aligned with the plane of their parent pseudodisk, and orbital motion following the spin of this pseudodisk. On the other hand, formation by capture should produce protostellar systems with randomly aligned disks and orbits, as well as large orbital eccentricities.

Our ability to distinguish between competing formation models is hampered by the difficulty in studying and therefore elucidating the properties of multiple protostellar systems. The average separation of binary or hierarchical pairs in multiple systems at the pre-main sequence and main sequence is $\sim$40 AU (Duquennoy & Mayor 1991; Mathieu 1994), corresponding to an angular separation of just $\sim 0\farcs3$ at the distance of the nearest active star-forming regions at $\sim$140 pc. The circumstellar disks of individual protostellar components are expected to be truncated by mutual gravitational interactions to no larger than about one-third the orbital separation (Artymowicz & Lubow 1994; Pichardo et al. 2005), and hence resolving these disks requires angular resolutions higher than $\sim 0\farcs1$. At the present time, the only telescope able to penetrate the molecular gas and dust surrounding protostellar systems and detect their individual components at such high angular resolutions is the Very Large Array (VLA).

One of the most intensively and best studied of all known multiple protostellar systems is L1551 IRS 5. This optically invisible object was discovered by Strom et al. (1976) in a near-IR survey of the LDN 1551 cloud, which is part of a network of molecular clouds at a distance of $\sim$140 pc (Kenyon et al. 1994) in the constellation Taurus. L1551 IRS 5 is associated with the first recognized bipolar molecular outflow (Snell et al. 1980), now known to be ubiquitous around protostars. Bieging & Cohen (1985) discovered two sources at 2 cm in L1551 IRS 5, providing the first evidence for its duplicity. Rodríguez et al. (2003b) have since showed that the emission at centimeter wavelengths is produced by a pair of closely aligned (within $\sim 12^{\circ}$) bipolar ionized jets, which themselves are aligned with the larger scale bipolar molecular outflow. Looney et al. (1997) showed that the dust emission of L1551 IRS 5 at 3 mm originates from two closely separated components surrounded by a possible circumbinary disk, which itself is embedded in a larger scale dust envelope. Using the VLA at 7 mm, Rodríguez et al. (1998) resolved the two central components and showed that they are associated with

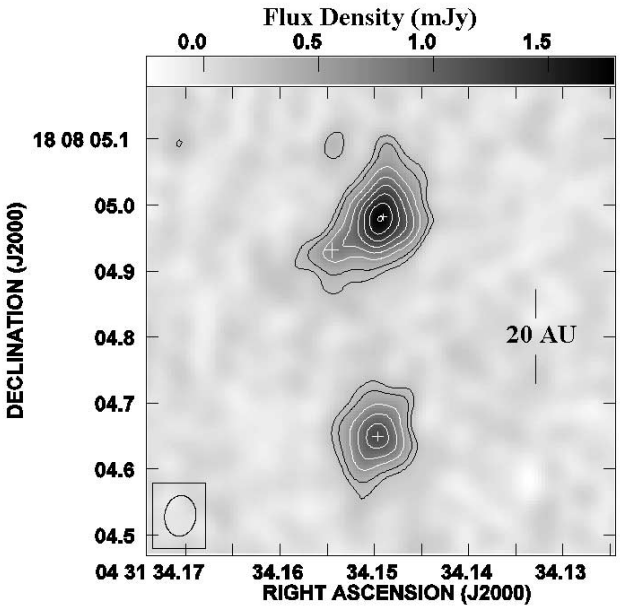

FIG. 1.—Image of L1551 IRS 5 at 7 mm, made with the VLA in A configuration on 2002 February 2. Produced with natural weighting, this image has a rms noise level (σ) of 0.118 mJy beam^{-1}. The FWHM of the synthesized beam is $0\farcs063 \times 0\farcs047$ (8.8×6.6 AU) at a P.A. of $-7\fdg38$ (measured anticlockwise from north), as shown in the lower left corner. Contour levels are plotted at -2, 2, 3, 5, 7, . . . , 15 σ. The plus signs mark the peak positions of the three components more clearly separated in our higher resolution images (Fig. 2) and listed in Table 1. To make the plus signs clearly visible, they are plotted with arm lengths corresponding to their ± 8 σ positional uncertainties. [*See the electronic edition of the Journal for a color version of this figure.*]

the two bipolar ionized jets. They attributed these components to dust emission from circumstellar disks.

The observation by Rodríguez et al. (1998) was made in 1997 when just 13 antennas of the VLA were equipped with receivers operating at 7 mm. The putative circumstellar disks were only partially resolved, and confusion from any detectable ionized jets was difficult to ascertain. Here, we present our observation of L1551 IRS 5 made with the full complement of the VLA equipped with receivers operating at 7 mm, providing a significant improvement in sensitivity. In addition, we used the Pie Town (PT) antenna of the Very Long Baseline Array (VLBA), linked in real time to the VLA, to provide a significant improvement in angular resolution. The images presented here have angular resolutions as high as $0\farcs037$, corresponding to a spatial resolution of just $\sim$5 AU at the distance of L1551 IRS 5. To appreciate the dramatic improvement in clarity, we invite the reader to compare the image shown in Figure 1 of Rodríguez et al. (1998) with those shown here in Figures 1 and 2.

Readers interested in the technical aspects of the observation and data reduction should now proceed to § 2. Those interested only in the results can skip to § 3. Readers interested to see how we use the results to elucidate various aspects of the system, including their likely formation pathway, should then continue to § 4. Those interested only in a concise summary of the results and their implications can proceed directly to § 4.5.

2. OBSERVATIONS AND DATA REDUCTION

We observed L1551 IRS 5 using the full complement of the VLA of the National Radio Astronomy Observatory (NRAO)[1] in its highest angular resolution A configuration at a wavelength of 7 mm (43.3 GHz) on 2002 January 29 and February 2. We also used the PT antenna of the NRAO, linked in real time to the VLA, to approximately double the length of the longest available baselines. Imaging at 7 mm in A configuration, especially with the inclusion of the PT antenna, requires frequent observations of a nearby calibrator (a technique known as fast switching) to track rapid amplitude and, especially, phase variations induced by the Earth's atmosphere. For this purpose, we used the quasar 0431+175, which lies just $\sim 0\fdg6$ away from L1551 IRS 5, switching the telescope alternately between 0431+175 and L1551 IRS 5 with a cycle time of just 2.5 minutes. Observations at 7 mm also require regular checks of the pointing accuracy of each antenna; we derived pointing corrections every 40–50 minutes from scans of the quasar 0431+206, which lies $\sim 2\fdg5$ away from L1551 IRS 5. For absolute flux density calibration, we used the quasar 0713+438, which we assumed had a flux density of 0.29 Jy at 7 mm (43.3 GHz). The observation on each day spanned $\sim$5.5 hr, with an integration time on L1551 IRS 5 of $\sim$3.4 hr per day.

On January 29, the weather and therefore phase stability were too poor to produce a reliable image. The weather was much improved on February 2, although care was still needed to edit and calibrate the data and then assess the reliability of the image produced. When calibrating the data, we inspected how well we tracked the atmospheric phase variations from observations of 0431+175 and discarded those portions of the data for which the phase measurements were deemed discontinuous from one calibrator scan to the next. We then assessed the reliability of the image produced by imaging small time portions (each spanning $\sim$1 hr) of the remaining data separately. All but a small portion of this data produced mutually consistent images, and these portions were kept to produce the final image. Our resulting image has significantly higher sensitivity and angular resolution than that made in 1997 January 10 by Rodríguez et al. (1998) with just 13 of the 27 antennas of the VLA.

3. RESULTS

In Figure 1, we show our image of L1551 IRS 5 made with just the VLA (i.e., not including the PT antenna) to provide a comparison with the earlier image made by Rodríguez et al. (1998). Both of these images have nearly identical angular resolutions, with the synthesized beam (a two-dimensional Gaussian) in our image having a size at full width at half-maximum (FWHM) of $0\farcs063 \times 0\farcs047$ (8.8×6.6 AU). Our image, however, has a factor of 2 higher sensitivity, with a root mean square (rms) noise level of just 0.118 mJy beam^{-1}. In common with the image of Rodríguez et al. (1998), we find two compact components, hereafter referred to as the northern (N) and southern (S) components, separated by $\sim 0\farcs3$. The N component, however, exhibits an extension to the southeast that is not seen in the image of Rodríguez et al. (1998). This extension would have been right at the detection threshold (3 σ) of their image.

In Figure 2, we show our images of L1551 IRS 5 made with the VLA-PT after applying two different weightings to the data. The image made with natural weighting is shown on the left and has a synthesized beam of $0\farcs058 \times 0\farcs044$ (8.1×6.2 AU) and rms noise level of 0.112 mJy beam^{-1}. The image made with robust = 0.5 (hereafter referred to as robust) weighting is shown on the right and has a smaller synthesized beam of $0\farcs046 \times 0\farcs037$ (6.4×5.2 AU) but a higher rms noise level of 0.124 mJy beam^{-1}. At these higher angular resolutions (especially Fig. 2, *right*), the southeast extension of the N component can now be seen to be a separate feature separated by just $\sim 0\farcs09$ from the N component. Hereafter, we refer to this feature as the third (3rd) component. We derived the peak positions of the two main components from

[1] The NRAO is a facility of the National Science Foundation, operated under cooperative agreement by Associated Universities, Inc.

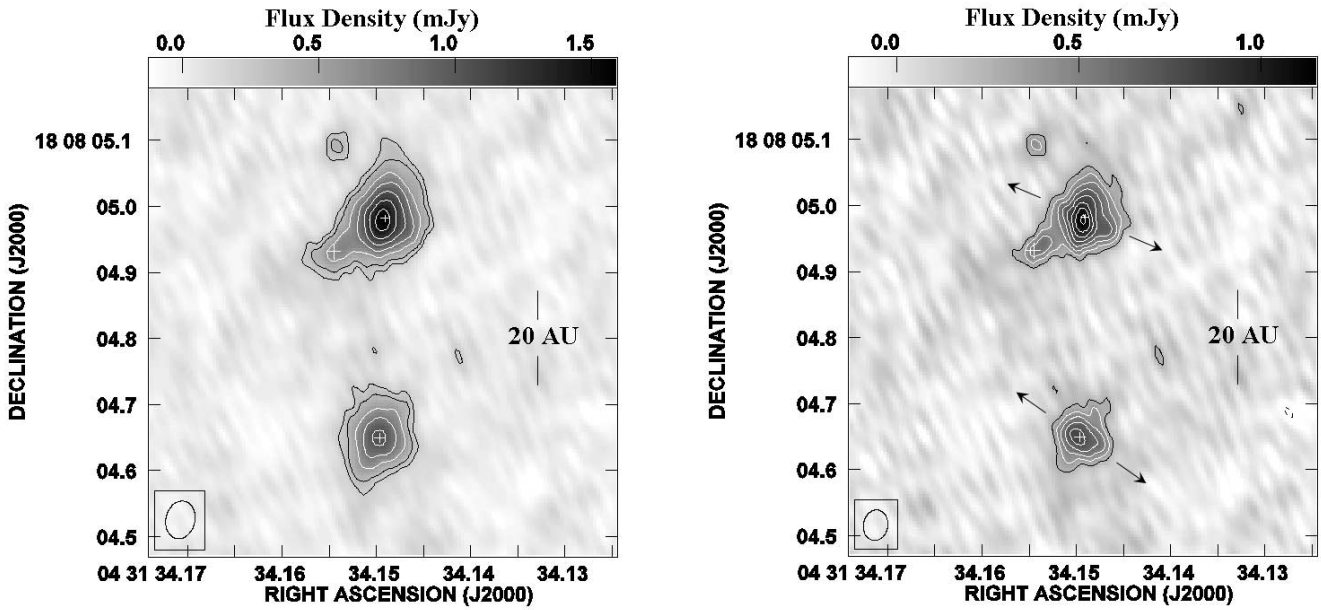

FIG. 2.—Same as Fig. 1, but with the addition of the PT antenna to increase the angular resolution. *Left*: Produced with natural weighting, this image has a rms noise level (σ) of 0.112 mJy beam^{-1}. The FWHM of the synthesized beam is $0''.058 \times 0''.044$ (8.1×6.2 AU) at P.A. $= -12°.9$, as shown in the lower left corner. Contour levels are plotted at $-3, -2, 2, 3, 5, 7, \ldots, 13\ \sigma$. The peak positions of the N and S components, indicated by plus signs and listed in Table 1, are derived from this image. *Right*: Produced using robust $= 0.5$ weighting, this image has a higher rms noise level of 0.124 mJy beam^{-1}, but smaller synthesized beam. The FWHM of the synthesized beam is $0''.046 \times 0''.037$ (6.4×5.2 AU) at P.A. $= -10°.2$, as shown in the lower left corner. Contour levels are plotted at $-3, -2, 2, 3, 4, \ldots, 9\ \sigma$. At this angular resolution, the N and S components each resemble a cross. One arm of each cross is aligned with the direction of a bipolar ionized jet imaged at 3.6 cm by Rodríguez et al. (2003b), as indicated by the two pairs of arrows. A third component is clearly separated from and lies to the southeast of the N component. [*See the electronic edition of the Journal for a color version of this figure.*]

the natural-weighted image (Fig. 2, *left*), which gives smaller positional uncertainties. To derive the peak position of the 3rd component, we first subtracted the N component from the image in the manner described in §§ 3.1 and 3.2. The peak positions of all three components are listed in Table 1 and are indicated by plus signs in all our figures.

Both the N and S components, but not the 3rd component, exhibit a crosslike structure. One arm of each cross is accurately aligned with the axis of a bipolar ionized jet (indicated by opposing arrows) associated with that component (Rodríguez et al. 2003b) and thus delineates the base of that jet. The other arm orthogonal to the jet presumably delineates a circumstellar dust disk. There is no known ionized jet along the major axis of the 3rd component, so we assume that this component also corresponds to a circumstellar dust disk. Our image therefore suggests that L1551 IRS 5 comprises three separate components and hence is a triple system.

TABLE 1

PEAK POSITIONS OF PROTOSTELLAR COMPONENTS

Component	R.A. (J2000.0)	Decl. (J2000.0)
N.....	04 31 34.14910 ± 0.00009[a]	+18 08 04.9818 ± 0.0016[b]
S	04 31 34.14967 ± 0.00012[a]	+18 08 04.6492 ± 0.0020[b]
3rd	04 31 34.15453 ± 0.00021[a]	+18 08 04.9317 ± 0.0026[b]

NOTES.—The peak positions of the N and S components were derived from the natural-weighted image in Fig. 2 (*left*). The peak position of the 3rd component was derived from the natural-weighted image in Fig. 4 (*right*), where the N component has been subtracted from the image. Units of right ascension are hours, minutes, and seconds, and units of declination are degrees, arcminutes, and arcseconds.

[a] Error given in seconds.

[b] Error given in arcseconds.

3.1. *Properties of the Bipolar Ionized Jets*

To properly determine the properties of the N and S disks, we first have to subtract the contribution from their bipolar ionized jets. From trial-and-error subtracting of model jets from the images in Figure 2, we found that a cleaner subtraction was produced by uniformly bright linear structures, rather than two-dimensional Gaussian structures, convolved with the synthesized beam. Subtracting Gaussian structures for both jets leaves a local minima at the center and a pinch at the waist of the disks, i.e., oversubtraction at the inner regions of the jet. The results after subtracting the best-fit, uniformly bright linear structures (convolved with the synthesized beam) from the natural- and robust-weighted images in Figure 2 are shown in Figure 3. Even this type of subtraction leaves a slight pinch at the waist of the N disk in the robust image of Figure 3, suggesting that at this angular resolution the N jet is better modeled as having two slightly brighter lobes.

In Table 2, we list the parameters (lengths, widths, and flux densities) of the linear structures that produced the cleanest subtraction of the jets as shown in Figure 3. We fixed their position angles to the values measured by Rodríguez et al. (2003b), who at 3.6 cm were able to trace both jets to a much larger extent and hence determine their position angles more accurately. Both jets are unresolved along their minor axes, and hence the upper limits on their widths correspond to the FWHM of the synthesized beam along the minor axes of the respective jets in the robust image. We found that values that differ by more than about ±10% in length or flux density from those listed produced noticeably poorer subtractions.

Our results place an upper limit of 6.4 and 6.2 AU, respectively, for the widths of the N and S jets. (The different upper limits for the widths of the two jets result from the slightly different position angles of their minor axes with respect to the noncircular synthesized

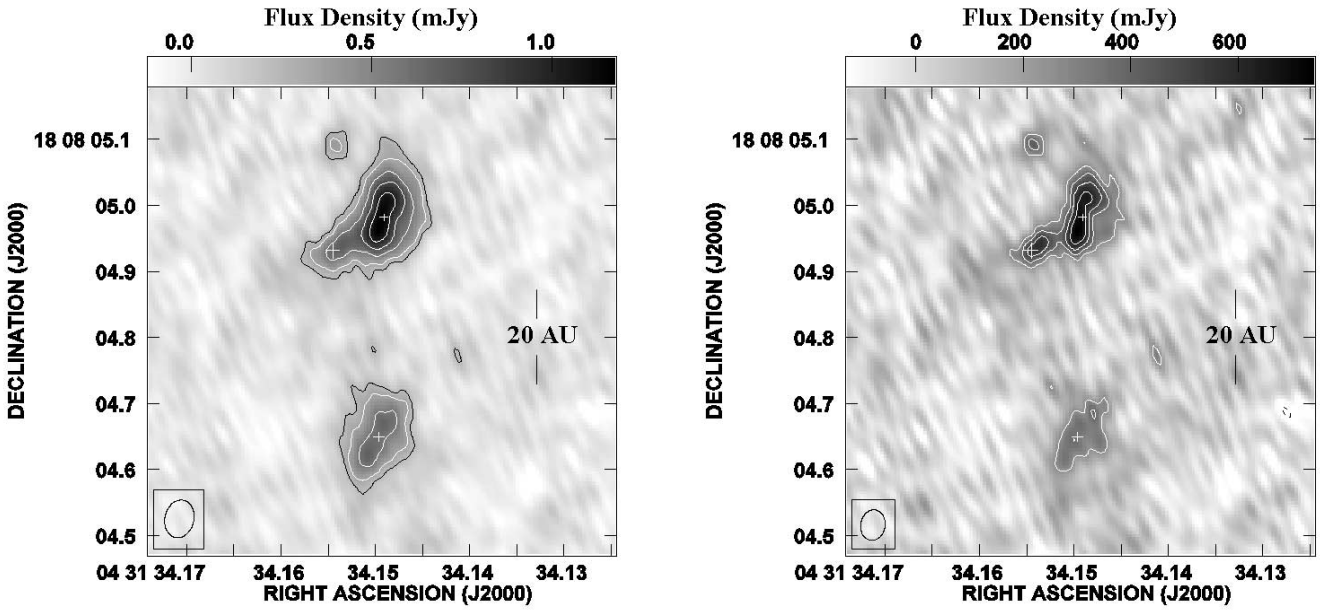

FIG. 3.—Same as Fig. 2, but with the two bipolar ionized jets subtracted in the manner described in the text, leaving only the circumstellar dust disks. *Left*: Produced with natural weighting, contour levels are plotted at -3, -2, 2, 3, 5, 7, . . . , 11 σ ($\sigma = 0.112$ mJy beam^{-1}). The properties of the S disk as listed in Table 3 are derived from this image. *Right*: Produced with robust = 0.5 weighting, contour levels are plotted at -3, -2, 2, 3, 4, and 5 σ ($\sigma = 0.124$ mJy beam^{-1}). [*See the electronic edition of the Journal for a color version of this figure.*]

beam.) These jets must therefore be collimated within a radial distance of just 3.1–3.2 AU from their central protostars.

3.2. *Properties of the Circumstellar Dust Disks*

After subtracting the bipolar ionized jets as described in § 3.1, we fitted two-dimensional Gaussians to each disk in order to derive their physical parameters (sizes along their major and minor axes at FWHM, position angles, flux densities, and brightness temperatures). We found that the parameters derived from the natural- and robust-weighted images were identical within measurement uncertainties, but the former (which has poorer angular resolution but lower noise level) had significantly smaller uncertainties. To better separate and hence properly derive the properties of the N and 3rd disks in the natural-weighted image, we first subtracted the 3rd disk from this image, using its parameters as derived from the robust-weighted image. The resulting image is shown in Figure 4 (*left*). After deriving the parameters of the N disk from this image, we subtracted the N disk from the natural-weighted image of Figure 3 to produce the image in Figure 4 (*right*). This image was used to more precisely determine the peak position of the 3rd component (as listed in Table 1) and the parameters of its disk.

TABLE 2
PARAMETERS OF BIPOLAR IONIZED JETS

Component	Length[a] (arcsec)	Width[a] (arcsec)	Flux Density (mJy)	P.A. (deg)
N.....	0.110 (15.4)	<0.046 (<6.4)	1.2	67 ± 3
S	0.080 (11.2)	<0.044 (<6.2)	0.9	55 ± 1

NOTES.—Uncertainty in length and flux density is estimated to be ~10% (see text). The upper limit on the width corresponds to FWHM of the synthesized beam in our robust = 0.5 image along the minor axis of each jet. Position angles are measured anticlockwise from north and are taken from Rodríguez et al. (2003b).

[a] The value given in parentheses is in AU.

The inferred parameters of the disks are listed in Table 3. All these parameters were derived from the natural-weighted images of Figures 3 and 4, except for the upper limit on the size of the 3rd disk along its minor axis. The latter is derived from the robust-weighted image of Figure 3 that has a higher angular resolution. The N disk has dimensions of (16.0 ± 0.7) × (8.1 ± 0.4) AU and position angle of 165° ± 3°, and the S disk has dimensions of (17.8 ± 1.3) × (9.5 ± 0.8) AU and position angle of 158° ± 5°. Both their dimensions and position angles are therefore similar to within measurement uncertainties (<1.6 σ). The flux density of the N disk, however, is significantly larger (by a factor of 1.4 ± 0.2) than that of the S disk. The brightness temperature of the N disk, 179 ± 17 K, is therefore higher than that of the S disk, 94 ± 8 K.

The major axes of the N and S disks have position angles that are quite accurately orthogonal to the axes of their corresponding bipolar ionized jets (as listed in Table 2). The orientation of the disk-jet axes differ by 98° ± 4° for the N component and by 103° ± 5° for the S component. Note that the orientations of both jets are inferred from features with dimensions of about 30–50 AU, whereas the disks have dimensions of <20 AU.

The 3rd disk has a size of 8.8 ± 1.1 AU along its major axis and is unresolved along its minor axis with a size of less than 5.9 AU. The position angle of this disk is 118° ± 8°, which is significantly different [by (40°–47°) ± 9°] from the position angles of the N and S disks. It also has a significantly smaller flux density than either the N or S disks. Because of its relatively small size, however, the lower limit on its brightness temperature of 96 ± 12 K is nevertheless comparable with the measured brightness temperature of the S disk.

3.3. *Relative Proper Motion*

Rodríguez et al. (2003a) have presented marginally significant evidence for a change in the separation and position angle between the N and S components with time. This evidence is based on observations with the VLA in A configuration at 2 cm between

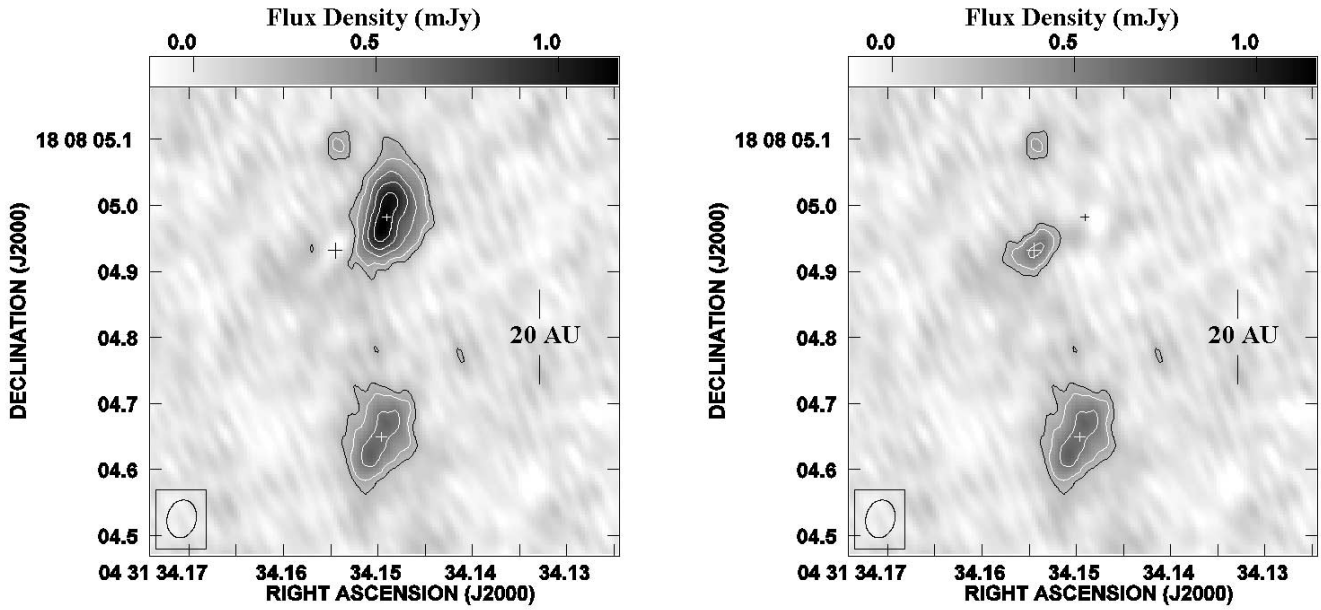

FIG. 4.—Same as Fig. 3 (*left*; natural weighting), but with the N and 3rd disks subtracted alternately to better determine their individual properties. *Left*: The 3rd disk subtracted. Contour levels are plotted at -3, -2, 2, 3, 5, 7, and 9 σ ($\sigma = 0.112$ mJy beam^{-1}). The properties of the N disk as listed in Table 3 are derived from this image. *Right*: The N disk subtracted. Contour levels are plotted at -3, -2, 2, 3, and 5 σ. The peak position of the 3rd component as marked by a plus sign and listed in Table 1 is derived from this image, as are the properties of this disk as listed in Table 3. [*See the electronic edition of the Journal for a color version of this figure*.]

1983.89 and 1998.41. In Table 4, we list the position of the S component relative to the N component at the time of our observation (epoch 2002.09), as derived from the natural-weighted image of Figure 2. The projected separation is $0\farcs333 \pm 0\farcs003$ (46.6 ± 0.4 AU), and the position angle is $178\fdg6 \pm 0\fdg4$. In Figure 5, we plot these values together with the earlier measurements reported by Rodríguez et al. (2003a), as well as the measurements by Rodríguez et al. (1998) at 7 mm (epoch 1997.03). The dashed lines are the least-squares fit that Rodríguez et al. (2003a) derived from their measurements. As can be seen, our measurements, which have significantly lower uncertainties owing to our higher angular resolution, confirm the trend of increasing separation and clockwise motion of the two components. The solid lines are the least-squares fit to all the measurements and give an annual change in separation of $\mu_{\rm sep} = +2.5 \pm 0.5$ mas yr^{-1} and position angle of $\mu_{\rm P.A.} = -0\fdg63 \pm 0\fdg19$ yr^{-1}.

In Figure 6, we plot the change in right ascension (R.A.) and declination (decl.) of the S component with respect to the N component from all the above-mentioned measurements. The diagonal solid lines are the least-squares fits to all the measurements. The annual change in R.A. is Δ(R.A.) $= -3.2 \pm 0.9$ mas yr^{-1} and decl. is Δ(decl.) $= -2.6 \pm 0.7$ mas yr^{-1}, where negative values indicate motion toward the east and south relative to the N component. The S component is therefore moving at a projected tangential velocity of $v_t = 4.1 \pm 0.8$ mas yr^{-1} at a position angle of $v_{\rm P.A.} = 129^\circ \pm 11^\circ$ with respect to the N component.

As listed in Table 4 also, the projected separation between the N and 3rd components is $0\farcs092 \pm 0\farcs003$ (12.9 ± 0.4 AU). The position angle of the 3rd component measured from the N component is $122\fdg9 \pm 1\fdg9$.

4. DISCUSSION

4.1. *Orbital Geometries*

We resolve the N and S disks along both their major and minor axes. This allows us to infer their inclinations from the plane of the sky, provided that the disks are intrinsically circular and geometrically thin (in these cases, with thicknesses $\ll$9 AU). We find that the N disk has an inclination of $59^\circ \pm 2^\circ$ and that the S disk has $58^\circ \pm 4^\circ$, identical to within measurement uncertainties. As their major axes also share similar orientations in the sky (difference in position angles of $7^\circ \pm 6^\circ$; Table 3), the equatorial planes of the N and S disks must therefore be accurately parallel.

As a check, we compare the inferred inclination of the disks with that of their bipolar outflows. As the axes of the N and S bipolar ionized jets are quite accurately perpendicular to the major axes of their respective circumstellar disks (§ 3.2), we infer that both jets have an inclination from the plane of the sky of $\sim 60^\circ$.

TABLE 3
PARAMETERS OF CIRCUMSTELLAR DUST DISKS

Component	Major Axis[a] (arcsec)	Minor Axis[a] (arcsec)	P.A. (deg)	Flux Density (mJy)	Brightness Temperature (K)
N	0.114 ± 0.005 (16.0 ± 0.7)	0.058 ± 0.003 (8.1 ± 0.4)	165 ± 3	4.2 ± 0.3	179 ± 17
S	0.127 ± 0.009 (17.8 ± 1.3)	0.068 ± 0.006 (9.5 ± 0.8)	158 ± 5	2.9 ± 0.3	94 ± 8
3rd	0.063 ± 0.008 (8.8 ± 1.1)	<0.042 (<5.9)	118 ± 8	0.9 ± 0.1	$>96 \pm 12$

NOTES.—These parameters were derived by fitting two-dimensional Gaussian structures to each disk in the natural-weighted images of Figs. 3 and 4, except for the upper limit on the width of the 3rd disk. The latter corresponds to FWHM of the synthesized beam in the robust image of Fig. 3 along the minor axis of this disk.

[a] The value in parentheses is in AU.

TABLE 4
PEAK POSITIONS RELATIVE TO THE N COMPONENT AT EPOCH 2002.09

Component	Δ(R.A.) (mas)	Δ(Decl.) (mas)	Separation (mas)	P.A. (deg)
S	−8.2 ± 2.2	−332.6 ± 2.6	332.7 ± 2.6	178.6 ± 0.4
3rd	−77.4 ± 3.2	−50.1 ± 3.1	92.2 ± 3.2	122.9 ± 1.9

Based on a simple model, Liseau & Sandell (1986) inferred an inclination of 70° ± 5° for the axis of the large-scale bipolar (CO) molecular outflow from L1551 IRS 5. This is roughly consistent with the inclination that we infer for the radio jets. From a model for the knots (Herbig-Haro objects) in the optical jet, Stocke et al. (1988) inferred an inclination ranging from ≳15° to ∼45°, depending on the individual knots. Fridlund & Liseau (1994) found that the tangential velocities of the knots predicted by the model of Stocke et al. (1988) were consistent with their measurements. Furthermore, they suggested that, taken together, the available measurements suggest an inclination of ∼30° for the axis of the optical jet. This is significantly smaller than the inclination we infer for the radio jets, but it should be borne in mind that the inferred inclination of the optical jet is model dependent.

In the following, we shall use as constraints the observed geometry and relative proper motion of the N and S components to constrain their possible orbital geometries. We consider both circular and elliptical—but only coplanar—orbits (i.e., orbital plane aligned with the plane of the disks). We implicitly assume that the 3rd component, which is likely the least massive component (see § 4.2.1), has a negligible effect on the orbits of its more massive companions.

4.1.1. *Circular Orbits*

We consider here a circular coplanar orbit with an orbital geometry as illustrated in Figure 7. The N component is held fixed, with the S component moving in a deprojected circular orbit about the N component. The orbital plane is inclined by 59° ± 2° from the plane of the sky (the inclination of the N disk), and its projected major axis is aligned with the major axis of the N disk. For a clockwise orbital motion as is observed, the S component should therefore be closely approaching (within a projected/deprojected angular separation of 14° ± 3°/26° ± 5° from) its maximum projected separation from the N component, when the major axes of both disks become aligned. This is consistent with the measured increase in separation between the N and S components with time.

More specifically, for a circular coplanar orbit with an inclination of 59° ± 2°, the predicted space motion of the S component is toward a position angle of $v_{\rm P.A.} = 118° \pm 8°$ with respect to the N component. This is consistent with that measured of $v_{\rm P.A.} = 129° \pm 11°$. Given the rate of change in position angle of the S relative to the N components of $\mu_{\rm P.A.} = -0\overset{\circ}{.}63 \pm 0\overset{\circ}{.}19$ yr^{-1}, the predicted rate of change in their separation is $\mu_{\rm sep} = +2.0 \pm 0.7$ mas yr^{-1}. This again is consistent with that measured of $\mu_{\rm sep} = +2.5 \pm 0.5$ mas yr^{-1}. The measured projected separation of 46.6 ± 0.4 AU then implies a true orbital radius of 50.2 ± 1.7 AU. The deprojected orbital velocity of the S component with respect to the N component is 6 ± 1 mas yr^{-1}, corresponding to 4.0 ± 0.8 km s^{-1}. The orbital period is therefore 377 ± 79 yr, and the total mass of the system is 0.89 ± 0.26 $M_\odot$.

4.1.2. *Elliptical Orbits*

Coplanar elliptical orbits also are permitted within the current precision of the measured relative proper motion. As we shall see, the range of permitted orbital solutions is larger for smaller eccentricities. The orbital geometry is illustrated in Figure 8, where the N component (held fixed) now lies at one of the focii of the deprojected elliptical orbit of the S component. Unlike for circular orbits, the projected major axis of the elliptical orbit need not be parallel with the major axes of the disks; we parameterize this angle as θ. As before, the orbital inclination is 59° ± 2°. For a given eccentricity e, we determine the range over which θ results in a relative proper motion ($v_{\rm P.A.}$ and $\mu_{\rm sep}$) that is similar to that measured within a difference of ±2 σ. Two families of solutions are allowed, depending on whether the S component is closer to apastron or periastron. For these two families, positive values of θ indicate that the S component is approaching apastron (case I below) or periastron (case II), respectively; $\theta = 0$ indicates that the S component is at apastron or periastron.

Case I: approaching apastron.—Let us first consider the case where the S component is closer to apastron. The permitted orbital solutions (θ and deprojected semimajor axis, a, of the orbit) are tabulated in Table 5 for eccentricities in the range 0.2–0.8.

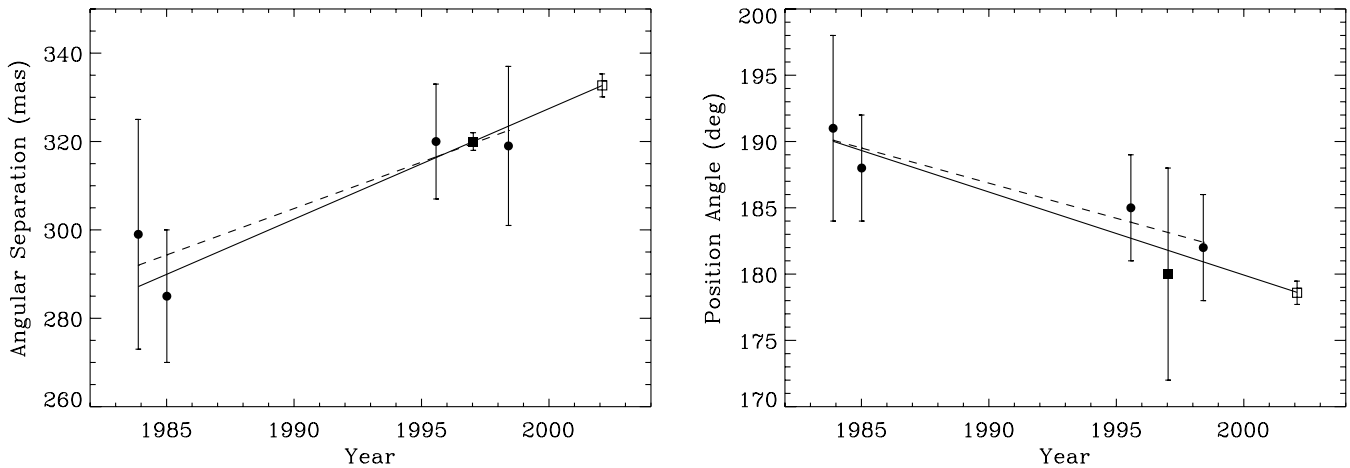

FIG. 5.—Proper motion of the S relative to the N component. *Left*: Angular separation at six different epochs, as described in the text. Filled circles are measurements at 2 cm compiled by Rodríguez et al. (2003a), the filled square at 7 mm by Rodríguez et al. (1998), and the open square at 7 mm reported here. The error bars correspond to ±1 σ uncertainty. *Right*: Position angle at the same six epochs. The dashed lines are fits to the filled circles, as reported by Rodríguez et al. (2003a), and solid lines are our least-squares fits to all the measurements. The latter gives an annual change in separation of $\mu_{\rm sep} = +2.5 \pm 0.5$ mas yr^{-1} and position angle of $\mu_{\rm P.A.} = -0\overset{\circ}{.}63 \pm 0\overset{\circ}{.}19$ yr^{-1}.

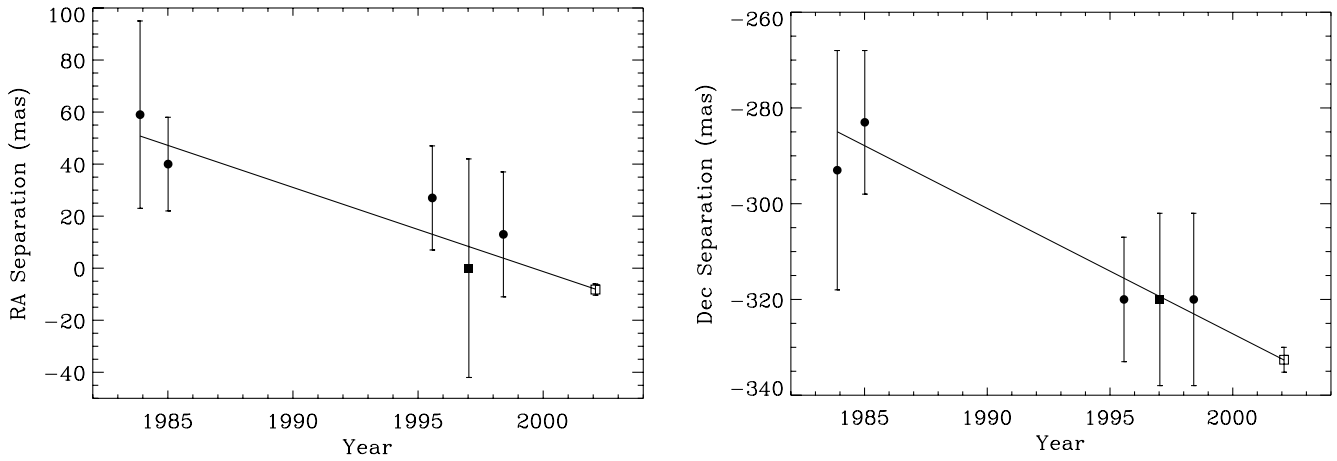

FIG. 6.—Proper motion of the S relative to the N component, as in Fig. 5. *Left*: Separation in R.A. at six epochs. *Right*: Separation in decl. at the same six epochs. The solid lines are the least-squares fits and give an annual change in R.A. of $\Delta(\mathrm{R.A.}) = -3.2 \pm 0.9$ mas yr^{-1} and in decl. of $\Delta(\mathrm{decl.}) = -2.6 \pm 0.7$ mas yr^{-1}. Motion toward increasingly smaller values indicates movement toward the east and south with respect to the N component.

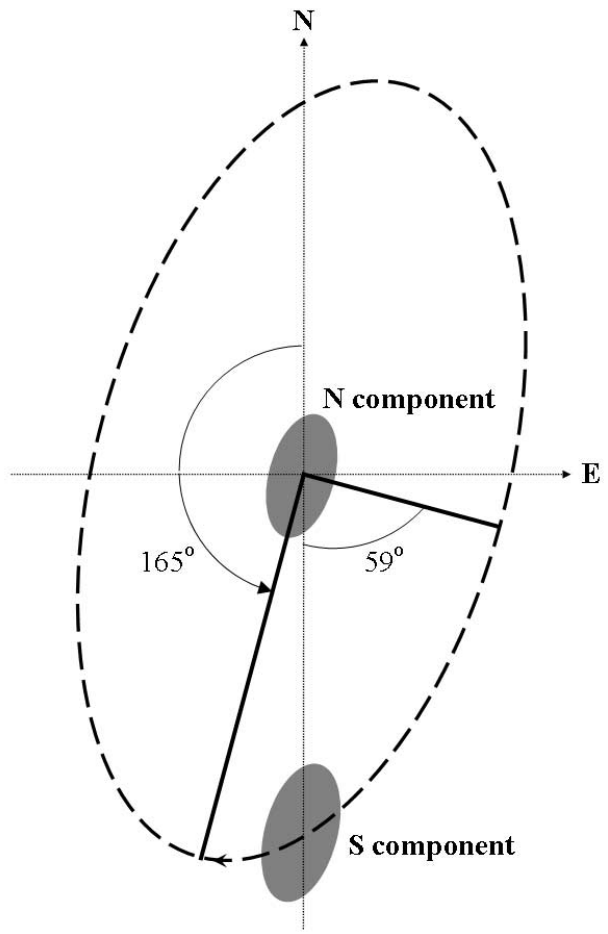

FIG. 7.—Schematic of a circular orbit inclined by 59° to the plane of the sky, resulting in a projected elliptical orbit. The semimajor and semiminor axes of the orbit are indicated by thick lines. The orbital inclination corresponds to the inferred disk inclinations of the N and S components (i.e., coplanar orbit). The projected major axis of the orbit lies at a position angle of 165°, same as that for the disk of the N component. This component is held fixed at the center of the orbit, with the clockwise orbital motion of the S component indicated by the dashed line. The dimensions of the two circumstellar disks relative to that inferred for the orbit (see text) are drawn to scale.

(The predicted maximum sizes of the circumstellar disks and minimum size of the circumbinary gap also are listed in this table, and discussed in § 4.2.) We find that the allowable range in θ is quite small and narrows as the eccentricity increases, e.g., from 8°–35° for $e = 0.2$ to just 2°–4° for $e = 0.8$. The parameter space of possible solutions is therefore larger for smaller eccentricities. Regardless of the eccentricity, the only permitted orbits are those for which the S component is approaching rather than receding from apastron (i.e., $\theta > 0°$).

As shown in Table 5, the deprojected semimajor axes of allowed orbits decrease (for a given θ) as the eccentricity increases, e.g., from 40–59 AU for $e = 0.2$ to 26–29 AU for $e = 0.8$. The orbital separation at periastron, $(1 - e)a$, therefore decreases as the eccentricity increases, and becomes comparable to or smaller than the disk sizes at $e \gtrsim 0.5$. Indeed, as we shall show in § 4.2.2, eccentricities $e \gtrsim 0.3$ are not allowed, as the predicted maximum sizes of the N and S disks, truncated by mutual gravitational interactions between their central protostars, become smaller than their observed sizes.

Case II: approaching periastron.—Let us now consider the case where the S component is closer to periastron. The permitted orbital solutions (along with the predicted maximum sizes of the circumstellar disks and minimum size of the circumbinary gap discussed in § 4.2) are tabulated in Table 6 for eccentricities in the range 0.2–0.8. Like before, we find that the allowable range in θ decreases as the eccentricity increases, although for the same eccentricity this range is now larger, e.g., from 12°–48° for $e = 0.2$ to 18°–31° for $e = 0.8$. Once again, the parameter space of possible solutions is larger for smaller eccentricities. Regardless of the eccentricity, in this case the only permitted orbits are those for which the S component is approaching rather than receding from periastron (i.e., $\theta > 0°$).

As shown in Table 6, unlike before, the deprojected semimajor axes of allowed orbits increase (for a given θ) as the eccentricity increases, e.g., from 61–84 AU for $e = 0.2$ to 244–259 AU for $e = 0.8$. The orbital separation is always much larger than the disk sizes, even at periastron. Indeed, we find that the predicted maximum sizes of the N and S disks are larger than their observed sizes for eccentricities as large as $e \approx 0.9$ (§ 4.2.2). On the other hand, as we shall show in § 4.2.3, eccentricities $e \gtrsim 0.3$ are not allowed because the predicted minimum size of the gap driven by the protostellar components into their surrounding natal material becomes larger than any such existing gap.

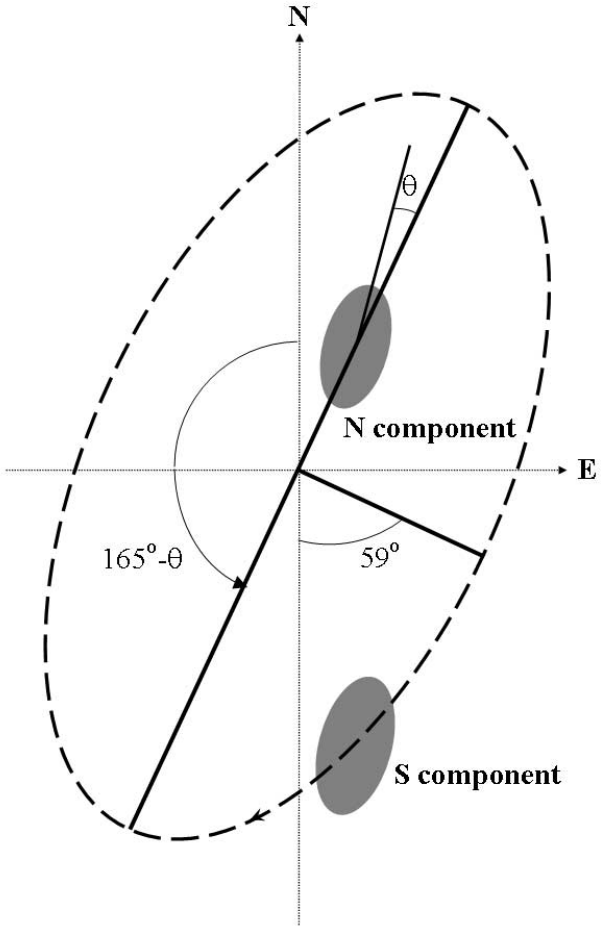

FIG. 8.—Schematic of an elliptical orbit inclined by 59° to the plane of the sky, resulting in a different projected elliptical orbit. The major and semiminor axes of the orbit are indicated by thick lines. The orbital inclination corresponds to the inferred disk inclinations of the N and S components (i.e., coplanar orbit). The projected major axis of the orbit lies at a position angle of $165^\circ - \theta$, i.e., making an angle θ to the major axis of the N disk. The N component, which is held fixed, lies at one of the focii of the deprojected elliptical orbit (but not at the focii of the projected elliptical orbit). The clockwise orbital motion of the S component is indicated by the dashed line. Positive values of θ correspond to the S component approaching (rather than receding from) either apastron or periastron.

TABLE 5
ALLOWED ORBITAL SOLUTIONS AND BINARY PROPERTIES FOR CASE I

Eccentricity (e)	θ (deg)	Orbital Semimajor Axis (AU)	Maximum Diameters Circumstellar Disks (AU)	Minimum Radius Circumbinary Gap (AU)
0.2.....	8–35	40–59	17.1–25.2	108–159
0.3.....	7–20	37–44	13.2–15.8	104–123
0.4.....	6–15	34–39	10.1–11.4	99–113
0.6.....	4–9	30–32	5.8–6.2	102–109
0.8.....	2–4	26–27	1.9–2.0	88–92

NOTES.—The computations of Pichardo et al. (2005) predict a maximum radius for the circumstellar disks of equal-mass binary components of $0.213a$ for $e = 0.2$, $0.178a$ for $e = 0.3$, $0.147a$ for $e = 0.4$, $0.097a$ for $e = 0.6$, and $0.037a$ for $e = 0.8$, where a is the semimajor axis of the binary orbit. The predicted minimum radius of the circumbinary gap is $2.7a$ for $e = 0.2$, $2.8a$ for $e = 0.3$, $2.9a$ for $e = 0.4$, $3.4a$ for $e = 0.6$, and $3.4a$ for $e = 0.8$.

TABLE 6
ALLOWED ORBITAL SOLUTIONS AND BINARY PROPERTIES FOR CASE II

Eccentricity (e)	θ (deg)	Orbital Semimajor Axis (AU)	Maximum Diameters Circumstellar Disks (AU)	Minimum Radius Circumbinary Gap (AU)
0.2.....	12–48	61–84	25.9–35.6	165–227
0.3.....	13–43	70–89	24.8–31.6	196–249
0.4.....	14–40	81–98	23.9–28.9	235–284
0.6.....	16–34	122–136	23.7–26.3	415–462
0.8.....	18–31	244–259	18.0–19.2	830–881

NOTES.—The computations of Pichardo et al. (2005) predict a maximum radius for the circumstellar disks of equal-mass binary components of $0.213a$ for $e = 0.2$, $0.178a$ for $e = 0.3$, $0.147a$ for $e = 0.4$, $0.097a$ for $e = 0.6$, and $0.037a$ for $e = 0.8$, where a is the semimajor axis of the binary orbit. The predicted minimum radius of the circumbinary gap is $2.7a$ for $e = 0.2$, $2.8a$ for $e = 0.3$, $2.9a$ for $e = 0.4$, $3.4a$ for $e = 0.6$, and $3.4a$ for $e = 0.8$.

Although we have considered only coplanar orbits, we note that tilted circular or elliptical orbits also can satisfy the constraints placed by the measured relative proper motion. As explained in § 4.3, any tilts (as long as they are relatively small) in the orbit do not change, and indeed are not unexpected in the context of, the formation scenario we propose for the N and S components.

4.2. *Circumstellar Disks and Circumbinary Gap*

Gravitational interactions between components of a binary (or multiple) system can truncate the circumstellar disks of their individual components, as well as drive surrounding material outward to create a circumbinary gap (Artymowicz & Lubow 1994). Pichardo et al. (2005) have computed the largest nonintersecting orbit in the individual circumstellar disks of binary systems that have arbitrary mass ratios and orbital eccentricities, as well as the smallest nonintersecting orbit of their circumbinary disk. They considered the case where the disks of both components lie in the orbital plane of the system (i.e., coplanar orbits), and where the individual protostellar masses dominate their corresponding disk masses. These calculations place stringent limits on the maximum radii of circumstellar disks and the minimum radii of circumbinary disks (with stable orbits) in such binary systems.

We shall now apply the computations of Pichardo et al. (2005) to L1551 IRS 5, assuming as before that the N and S components have a coplanar orbit and that the effects of the 3rd component can be ignored. In the following, we first use the measured disk sizes of the different components to constrain their individual protostellar masses. We then use the predicted maximum disk sizes, and predicted minimum size of the circumbinary gap, to constrain the eccentricities of elliptical orbits.

4.2.1. *Protostellar Masses*

If the circumstellar disks of the individual components of a binary system have sizes corresponding to their largest nonintersecting orbits, then their relative sizes are directly related to their relative protostellar masses. As both the N and S components have similar disk sizes, they presumably have similar protostellar masses. The ratio in size of their major axes of 0.90 ± 0.07 implies, for a circular orbit, a fractional protostellar mass in the N component of 0.45 ± 0.04. As the total mass of the N and S components is $0.89 \pm 0.26\ M_\odot$ (§ 4.1.1), this implies individual protostellar masses of about 0.4–0.5 $M_\odot$. These protostellar masses are about an order of magnitude or more larger than their individual disk masses, estimated to lie in the range 0.01–0.06 $M_\odot$ (Looney et al. 1997; Rodríguez et al. 1998).

As the disk of the 3rd component is tilted with respect to both the N and S components, the computations of Pichardo et al. (2005) cannot be strictly applied to this component. Their computations may nevertheless provide a crude estimate of the protostellar mass of the 3rd component. If this component is in a circular orbit around the N component, then the ratio in size of their major axes of $\sim$0.55 indicates a fractional protostellar mass in the 3rd component of $\sim$0.25. With a protostellar mass of $\sim$0.4 $M_{\odot}$ for the N component, the protostellar mass of the 3rd component is therefore $\sim$0.1 $M_{\odot}$. For an eccentric orbit, the corresponding protostellar mass of the 3rd component is smaller.

4.2.2. *Disk Truncation*

Pichardo et al. (2005) found that equal-mass protostellar components in a circular orbit should have a maximum disk radius of $\sim$0.257a, where a is the orbital semimajor axis (in this case, orbital radius). If the N and S components are in a circular orbit, their orbital radius is 50.2 $\pm$ 1.7 AU (§ 4.1.1) and hence the predicted maximum radii (diameters) of their disks are 12.9 $\pm$ 0.4 AU (25.8 $\pm$ 0.8 AU). The measured diameters of the N and S disks of 16.0 $\pm$ 0.7 and 17.8 $\pm$ 1.3 AU, respectively, are significantly smaller than their predicted maximal extents. Recall, however, that their measured sizes correspond to the FWHM of two-dimensional Gaussian functions fitted to the observed intensity profiles of the disks. The actual maximal extent of the disks may therefore be larger. In addition, their outermost regions may be below our detection threshold.

The measured (minimum) disk sizes of the N and S components can be used to place further constraints on their allowed elliptical orbits (§ 4.1.2). For a given mass ratio between components and a given orbital semimajor axis, the predicted maximum sizes of their individual disks are smaller for larger eccentricities, as the components are now closer along a part of their orbit. In Table 5, we tabulate the predicted maximum disk diameters for equal-mass components (i.e., same disk sizes) with orbits corresponding to the case where the S component is approaching apastron (case I in § 4.1.2). Because the semimajor axes of permitted orbits decrease (for a given θ) as the eccentricity increases, the predicted maximum disk sizes also decrease with increasing eccentricity. For an eccentricity $e = 0.3$, the predicted maximum disk diameters of 13–16 AU (0.178a) are smaller than or just compatible with the measured disk diameters of 16–18 AU. Thus, in the situation where the S component is approaching apastron, permissible elliptical orbits are constrained to eccentricities $e \lesssim 0.3$. If, as mentioned above, the true maximal extents of the disks are larger, the allowed orbital eccentricity is even smaller.

In Table 6, we tabulate the predicted maximum disk diameters for equal-mass components with orbits corresponding to the case where the S component is approaching periastron (case II in § 4.1.2). In this case, because the semimajor axes of permitted orbits increase dramatically with increasing eccentricity, the predicted maximum disk sizes are larger than their measured sizes over the range of eccentricities tabulated (up to $e = 0.8$). Indeed, we find that the predicted maximum disk sizes are larger than the measured disk sizes (for at least some allowed values of θ) for eccentricities as large as $e \approx 0.9$. On the other hand, as we show next (§ 4.2.3), at eccentricities $e \gtrsim 0.3$, the predicted size of the circumbinary gap driven by the N and S components is larger than the upper limit placed on any such gap.

We now use the measured disk size of the 3rd component to place a crude constraint on its minimum orbital radius. As before, we assume that this component is in a circular orbit about the N component. Then, as we showed in § 4.2.1, the fractional protostellar mass in the 3rd component is $\sim$0.25. The predicted maximum radius of its disk is $\sim$0.192a; for a disk diameter of 9 AU, the orbital radius is therefore $\sim$23 AU. The latter is much larger than the observed projected separation between the 3rd and N components of $\sim$13 AU. If the orbit is eccentric, the fractional protostellar mass in the 3rd component is smaller (§ 4.2.1), and the semimajor axis of its orbit is larger.

4.2.3. *Circumbinary Gap*

Pichardo et al. (2005) found that the minimum size of the gap driven by the binary components into the disk surrounding the entire system is only weakly dependent on the relative component masses. This central gap becomes larger in size as the eccentricity increases, but remains approximately circular irrespective of the orbital eccentricity. The predicted radius of the circumbinary gap for equal-mass components in a circular orbit is $\sim$2.0a and increases to $\sim$3.4a for an orbital eccentricity of $e = 0.8$. If the N and S components are in a circular orbit, then their orbital radius of 50.2 $\pm$ 1.7 AU (§ 4.1.1) translates into a minimum radius for their circumbinary gap of $\sim$100 AU ($\sim$0.″7). At an inclination of $\sim$60°, the gap would appear to have a size of about 200 $\times$ 100 AU (1.″4 $\times$ 0.″7) along its major and minor axes, and a position angle of $\sim$160°.

As described in more detail in the next section (§ 4.3), the entire L1551 IRS 5 system is surrounded by a rotating disk of molecular gas and dust (hereafter referred to as a circumbinary disk, although perhaps more accurately a circumtriple disk). The inner regions of this circumbinary dust disk have been imaged by Looney et al. (1997) at 3 mm with an angular resolution as high as $\sim$0.″5. They did not report any detection of a gap between the circumbinary and circumstellar disks, although any such gap would be difficult to discern in the presence of the bright circumstellar disks. An examination of the measured visibilities suggests that the circumbinary disk "is evident as the excess emission between 30 kλ and 90 kλ," corresponding to spatial scales of about 3″–8″ (Looney et al. 1997). Thus, the maximum diameter of any such gap is $\sim$400 AU ($\sim$3″), only a factor of $\sim$2 larger than the predicted minimum size of the circumbinary gap for a circular orbit. Takakuwa et al. (2004) have imaged the circumbinary disk of L1551 IRS 5 in both dust and molecular gas (CS $J = 7 \rightarrow 6$) at 0.8 mm with an angular resolution of 2″–3″. They find a rotating disk of molecular gas with a diameter of $\sim$400 AU ($\sim$3″). Any central gap in the circumbinary disk must therefore be significantly smaller.

From the above-mentioned observations, we place a conservative upper limit of 200 AU (1.″5) on the radius of any central gap in the circumbinary disk. As mentioned earlier, the predicted radius of the circumbinary gap in the case where the N and S components are in a circular orbit is $\sim$100 AU, a factor of $\sim$2 smaller than the inferred upper limit. In the case where they are in an elliptical orbit, this upper limit can be used to place further constraints on their allowed orbital eccentricities. In Table 5, we tabulate the predicted minimum radii of circumbinary gaps for equal-mass components with orbits corresponding to the case where the S component is approaching apastron (case I in § 4.1.2). As can be seen, the predicted minimum radius of the circumbinary gap is always comfortably smaller than the inferred upper limit of $\sim$200 AU over the range of eccentricities tabulated (as well as $e < 0.2$). In Table 6, we tabulate the predicted minimum radii of circumbinary gaps for equal-mass components with orbits corresponding to the case where the S component is approaching periastron (case II in § 4.1.2). In this case, because the semimajor axes of allowed orbits are larger than in the previous case, the predicted minimum radius of the circumbinary gap is comparable with the inferred upper limit of $\sim$200 AU even at small eccentricities.

Furthermore, because the semimajor axes of allowed orbits increase dramatically as the eccentricity increases, the predicted minimum radius of the circumbinary gap exceeds the inferred upper limit for $e > 0.3$. Thus, in the case where the S component is approaching periastron, only eccentricities $e \lesssim 0.3$ are allowed.

4.3. *Formation from Parent Molecular Condensation*

Momose et al. (1998) showed that L1551 IRS 5 lies at or close to the center of a rotating and contracting molecular condensation. As observed in $C^{18}O$ (1–0), this condensation has a diameter of ~2400 AU and can be modeled as a geometrically thin pseudodisk with its major axis at a position angle of $\sim 162^\circ$ and inclination to the plane of the sky of $\sim 64^\circ$. The pseudodisk exhibits clockwise rotation, as is confirmed by Takakuwa et al. (2004) from observations in CS (7–6) that trace the inner region of diameter ~400 AU.

As shown earlier, the N and S disks have similar position angles of $\sim 162^\circ$ (§ 3.2) and inclinations of $\sim 59^\circ$ (§ 4.1). Their orientation is therefore identical (within measurement uncertainties) to the orientation of the surrounding pseudodisk, implying that the equatorial planes of the circumstellar disks and pseudodisk are all parallel. In addition, the clockwise orbital motion of the N and S components resembles the clockwise rotational motion of the surrounding pseudodisk. Together with the relatively small upper limit we place on their orbital eccentricity (for coplanar orbits), these attributes firmly indicate that both the N and S components formed from their surrounding disklike condensation. Specifically, our results are in accord with the idea that these components formed via fragmentation in the central region of their parent pseudodisk. Such a mode of formation is expected to produce systems with circumstellar disks aligned with the plane of their parent pseudodisk, and orbital motion following the spin of this pseudodisk (e.g., see discussion and references in Bate et al. 2000). Although one might expect the orbital plane also to be aligned with the plane of the pseudodisk, small tilts are actually allowed, e.g., if one protostellar component formed above, and the other below, the midplane of the pseudodisk.

By contrast, formation by capture should preferentially form, at least initially, binary systems with randomly aligned disks and orbits, as well as large orbital eccentricities. Over time, the protostellar disks can become aligned by gravitational interactions between the binary components. Lubow & Ogilvie (2000) have looked at the case of binary systems with circular orbits and found that disks with radii significantly larger than $\sim 0.12a$ (where a is the orbital radius) can be quite quickly aligned by tidal torques (see also Bate et al. 2000). The N and S disks have radii of (at least) $\sim(0.16–0.18)a$ and, if originally misaligned, may therefore have become aligned by tidal torques. If so, they also are required to align with the plane of the surrounding disklike condensation. This could happen if the captured component is much less massive and hence its disk aligns with that of the more massive component, which formed from and whose disk is therefore aligned with the surrounding pseudodisk. As described in § 4.2.1, however, the N and S components appear to have essentially identical masses. Alternatively, the disks may have become aligned with the pseudodisk through the transfer of angular momentum from accreting material. The conditions under which such alignment can occur, and the timescale required, have not (to the best of our knowledge) been elucidated.

As mentioned above, formation by capture should result in large orbital eccentricities, perhaps contrary to the conservative upper limit of $e \approx 0.3$ for any eccentricity in the orbits (if coplanar) of the N and S components. Pre-main-sequence low-mass stars with orbital periods longer than ~10 days have been found to exhibit a broad range of eccentricities with values as large as $e \approx 0.8$ (Melo et al. 2001). On the other hand, all those with periods $\lesssim$10 days (circularization period) have essentially circular orbits ($e \lesssim 0.01$). The N and S components in L1551 IRS 5, with an orbital period of ~400 days (§ 4.1.1), would not have had time to circularize; instead, the 3rd component may be pumping up their orbital eccentricity. Their relatively small orbital eccentricity (if any) therefore argues against formation by capture.

The origin of the 3rd component is less clear. The disk of the 3rd component is not parallel with the N and S disks, nor with the surrounding disklike condensation. If this component also formed from the surrounding condensation, then its disk may have been misaligned by gravitational interactions with its (presumably) more massive companions. Indeed, the size of its disk is a factor of ~2 smaller than that of the N and S components and may therefore fall in the regime where tidal torques can misalign originally aligned disks (Lubow & Ogilvie 2000). On the other hand, we cannot at the present time rule out the possibility that this component was captured and is now accreting material from the surrounding pseudodisk. Smith et al. (1997) have investigated the stability of accreting triple protostellar systems. They find that, in the case (such as that applicable here) where the components have comparable masses, or where a hierarchical triple system in which the more closely separated components each have a higher mass than their more distant companion, accretion of material (with nonzero angular momentum) helps to stabilize the system.

4.4. *Outflow and Accretion*

Rodríguez et al. (2003b) showed that L1551 IRS 5 possesses a pair of bipolar ionized jets that are quite closely aligned in the sky. In their image at 3.6 cm, which is dominated by free-free emission and probes spatial scales of $\gtrsim$15 AU, the two jets exhibit relatively bright central cores along with more extended linear features. The central cores of these jets coincide with the two main (N and S) components observed by Rodríguez et al. (1998) at 7 mm. Our image at 7 mm, probing spatial scales of $\gtrsim$5 AU, traces higher densities in the inner regions of the jet cores (Fig. 2). It confirms that both jets are accurately centered on, and aligned closely perpendicular to, their corresponding circumstellar dust disks.

In the image of Rodríguez et al. (2003b) at 3.6 cm, the core of the S jet has a higher flux density than that of the N jet. In our image at 7 mm, by contrast, the N jet has a higher flux density than the S jet. Although time variability cannot be ruled out, both of these observations were made (coincidentally) just 22 days apart. Rodríguez et al. (2003a) have compiled measurements of L1551 IRS 5 at 2 cm from 1983 to 1988, all made at spatial resolutions of ~15 AU (to measure the proper motion of the two sources; § 3.3). At this wavelength, the emission is likely dominated by free-free emission. Except for a relatively brief period during the late 1980s when the S jet was undergoing a major ejection event, the flux density of the N jet at 2 cm is higher than that of the S jet.

Based on the quite closely contemporaneous measurements at 3.6 cm by Rodríguez et al. (2003b) and 7 mm reported here, the N jet has a spectral index (α) of 0.53 ± 0.03 and the S jet has -0.15 ± 0.08 (where the flux density $S \propto \nu^\alpha$). The quoted uncertainties in the spectral indices include an estimated uncertainty of ~10% in the inferred flux densities of the jets at 7 mm. The available data therefore suggest that (usually) the N jet is optically thick to a shorter wavelength than the S jet, and that at wavelengths shorter than ~3.6 cm it has a higher flux density. This in turn implies that, for otherwise similar jet parameters, the N jet

has a higher mass-loss rate than the S jet. As the N disk has a factor of ~2 higher brightness temperature than the S disk (see Table 2), albeit similar dimensions, the N component also may have a higher mass-accretion rate. If the N protostellar component has a lower mass, as the evidence described in § 4.2.1 tentatively suggests, then at the present time both accretion and outflow appear to be stronger onto the secondary component. Many models of protobinary systems with unequal component masses show that accretion preferentially occurs onto the secondary component, driving the mass ratio of the system to unity (e.g., Artymowicz & Lubow 1996; Bate & Bonnell 1997). A more recent simulation by Ochi et al. (2005) for a protobinary system in a circular coplanar orbit, however, reached the opposite conclusion.

The 3rd disk has a diameter about a factor of 2 smaller than either the N or S disks. It has a brightness temperature that is at least as high as that of the S disk, suggesting that this component also is actively accreting. The 3rd component, however, exhibits no detectable jet, with an upper limit in flux density of 0.33 mJy (3 σ detection threshold) at 7 mm. For otherwise similar parameters, any outflow from the 3rd component must therefore have a mass-loss rate at least a factor of 3–4 lower than those of the N and S components.

In the observation of Rodríguez et al. (2003b) at 3.6 cm, the cores of the N and S jets are resolved along both their major and minor axes. These cores have deconvolved sizes along their minor axes of ~12 AU, much larger than the upper limit of ~6 AU placed in our observation at 7 mm. This suggests that, at 7 mm, we are tracing the inner denser regions of an ionized outflow that has a relatively broad opening angle at or near its base. The outflow, however, must be well collimated farther out, in order to produce the extended linear features of the jet. Shang et al. (2004) have modeled the core of the S jet as observed at 3.6 cm in the context of the *X*-wind model of Shu et al. (1994). This model predicts that protostellar outflows have an intrinsically wide opening angle, but a jetlike appearance in the radio because of a cylindrical-like stratification in column density. Shang et al. (2004) were able to reproduce the observed size of the core at 3.6 cm along its major axis, and its radial variation in intensity within the inner regions. The model outflow, however, is not resolved along its minor axis, contrary to what is observed.

Shang et al. (2004) attributed the extended emission along the minor axis of the core at 3.6 cm to shock interactions between the wide-angle outflows of the two protostars. Indeed, away from the cores, the directions of both jets deviate from the orientation of the major axes of their respective cores. Rodríguez et al. (2003b) attributed these deviations to shock interactions between the two outflows, which must therefore have intrinsically wide opening angles. If so, then such shock interactions should be even stronger closer to the base of the outflows, and because of the higher column density here produce even stronger emission at 3.6 cm. In this picture, the column density in the interaction region is too low to produce detectable free-free emission at 7 mm in our observation. The observed properties of the jets at 7 mm therefore better reflect their intrinsic properties. The challenge now is to see whether the *X*-wind model, or other models, can reproduce the measured properties of the two jets at both 3.6 cm and 7 mm.

4.5. *Summary and Conclusions*

We have imaged the circumstellar dust disks and bipolar ionized jets of the multiple protostellar system L1551 IRS 5 at a wavelength of 7 mm. Taking advantage of the nearly full complement of the Very Large Array (VLA) together with the Pie Town (PT) antenna, our image has a factor of ~2 higher equivalent sensitivity and angular resolution than the image previously presented by Rodríguez et al. (1998). It provides the sharpest view yet of the properties of this system. We confirm the presence of two components oriented approximately north-south, with an angular separation of ~0.″3. Furthermore, we show for the first time the following properties of the L1551 IRS 5 system as observed at 7 mm.

1. The two main (N and S) components each comprise a circumstellar dust disk and bipolar ionized jet, with major axes orthogonal to each other within measurement uncertainties of 2–3 σ.
2. A third (3rd) component, having a lower flux density than the two main components, lies ~0.″09 southeast of the N component. This component would not have been detectable, or just barely detectable, in the previous observation of Rodríguez et al. (1998). We identify this component as another circumstellar dust disk, making L1551 IRS 5 a triple protostellar system.
3. All three circumstellar dust disks are relatively small in size compared with those of single protostars. The disks of the N and S components have essentially identical dimensions of 16.0 ± 0.7 and 17.8 ± 1.3 AU, respectively, and the disk of the 3rd component has an even smaller dimension of 8.8 ± 1.1 AU (Table 3).
4. The disks of the two main (N and S) components are parallel with each other to within measurement uncertainties of several degrees. The disk of the 3rd component, however, is misaligned by at least (40°–47°) ± 9° with respect to the two main components.
5. All three circumstellar dust disks have relatively high brightness temperatures, which place a lower limit on their dust temperature. The brightness temperature of the S disk is 94 ± 8 K, the 3rd disk is in excess of 96 ± 12 K, and the N disk is 179 ± 17 K.
6. The bipolar ionized jets of the N and S components have widths of less than 6.2–6.4 AU (Table 2). They are therefore collimated within a radial distance of less than 3.1–3.2 AU of their central protostars.
7. The bipolar ionized jet of the N component is likely to be optically thick to a shorter wavelength, and its flux density higher at wavelengths shorter than ~3.6 cm, compared with the bipolar ionized jet of the S component. For otherwise similar jet properties, the mass-loss rate of the N jet is therefore higher than that of the S jet. Any mass loss from the 3rd component is at least a factor of 3–4 lower than that of the two detected jets.

Comparing with earlier measurements of the relative positions of the N and S components, we confirmed that the S component is moving (in projection on the plane of the sky) southeast relative to the N component. We more precisely determined their relative motion and computed for a circular coplanar orbit the orbital period and combined masses. We used the computations of Pichardo et al. (2005), who predicted the maximum sizes of binary circumstellar disks, and minimum size of their circumbinary gap as imposed by gravitational interactions, to estimate individual protostellar masses and place stringent constraints on any orbital eccentricities. In using these computations, we assumed that the 3rd component has a negligible effect on its more massive companions. We summarize the results obtained.

1. The measured annual change in separation is $\mu_{\rm sep} = +2.5 \pm 0.5$ mas yr^{-1} toward a position angle of $v_{\rm P.A.} = 129° \pm 11°$ as measured from the S component relative to the N component.
2. If the disks and orbital planes are aligned, the measured relative motion is consistent (<1 σ) with a circular orbit. If this is the case, then the true orbital separation of the N and S components is 50.2 ± 1.7 AU, their orbital period is 377 ± 79 yr, and

their total mass is $0.89 \pm 0.26\ M_{\odot}$. Their similar disk sizes indicate similar protostellar masses.

3. The measured relative motion does not rule out elliptical orbits. The range of permitted orbital solutions, however, is larger for smaller eccentricities. We showed that, if in an eccentric orbit, the two components must be approaching (rather than receding from) either apastron or periastron.

4. If in a circular coplanar orbit, the measured sizes of the N and S disks of 16–18 AU are smaller than their predicted maximum sizes of ~26 AU. We note that the measured sizes may underestimate the true sizes of the N and S disks if, for example, the outer regions of the disks lie below our detection threshold. The same predictions place a conservative upper limit of $e \approx 0.3$ on any orbital eccentricity if the two components are approaching apastron.

5. Gravitational interactions between the protostellar components and their surrounding molecular gas and dust condensation should drive a circumbinary gap into this condensation. Present observations (Looney et al. 1997; Momose et al. 1998; Takakuwa et al. 2004) place an upper limit of ~200 AU on the radius of any such gap. If in a circular orbit, the predicted minimum radius of the circumbinary gap driven by the N and S components is ~100 AU, in agreement with the observed upper limit. The same prediction places a conservative upper limit of $e \approx 0.3$ on any orbital eccentricity if the two components are approaching periastron.

6. We make a crude estimate for the protostellar mass of the 3rd component of at most $\sim 0.1\ M_{\odot}$, and its true orbital separation from the N component of at least ~23 AU.

We compared the orientation of the circumstellar disks, and orbital motion of the N and S components, to the orientation and rotational motion of their surrounding molecular gas and dust pseudodisk (Looney et al. 1997; Momose et al. 1998; Takakuwa et al. 2004). Their relationship, and consequences for their formation scenarios, are as follows.

1. The orientation of the N and S circumstellar disks is parallel (to within measurement uncertainties) with that of the surrounding pseudodisk. Furthermore, the clockwise orbital motion of these components resembles the clockwise rotational motion of the pseudodisk.

2. Our results are in accord with the simplest predictions of fragmentation, but in contrast with those of capture, for the formation of the N and S components. Specifically, fragmentation in the central region of their parent pseudodisk should produce systems with circumstellar disks aligned with the plane of their parent pseudodisk, and orbital motion following the spin of this pseudodisk. By contrast, formation by capture should form, at least initially, binary systems with randomly aligned disks and orbits, as well as large orbital eccentricities. Alignment of protostellar disks by tidal torques is possible, but to be aligned with the surrounding pseudodisk requires the captured component to be much less massive than the component that formed from the pseudodisk. This is contrary to the essentially identical masses we infer for the N and S components.

3. The origin of the 3rd component, whose disk plane is not aligned with either the N or S components or the surrounding pseudodisk, is at present unclear. Misalignment of this relatively small circumstellar disk by its more massive companions is possible. On the other hand, this component may have been captured.

Future observations of the (relative) proper motion of the 3rd component could help distinguish between the two abovementioned possibilities for its origin. Such observations also could provide a more precise measurement of the relative proper motion of the N and S components, and narrow the range of possible orbital eccentricities as well as any tilts between the disk and orbital planes.

J. Lim acknowledges support from the National Science Council of Taiwan for conducting this work.

Facilities: VLA

REFERENCES

Artymowicz, P., & Lubow, S. H. 1994, ApJ, 421, 651
———. 1996, ApJ, 467, L77
Bate, M. R., & Bonnell, I. A. 1997, MNRAS, 285, 33
Bate, M. R., Bonnell, I. A., Clarke, C. J., Lubow, S. H., Ogilvie, G. I., Pringle, J. E., & Tout, C. A. 2000, MNRAS, 317, 773
Bieging, J. H., & Cohen, M. 1985, ApJ, 289, L5
Duchêne, G., Delgado-Donate, E., Haisch, K. E., Jr., Loinard, L., & Rodríguez, L. F. 2006, Protostars and Planets V, ed. B. Reipurth, D. Jewitt, & K. Keil (Tucson: Univ. Arizona Press), in press
Duquennoy, A., & Mayor, M. 1991, A&A, 248, 485
Fridlund, C. V. M., & Liseau, R. 1994, A&A, 292, 631
Galli, D., & Shu, F. H. 1993, ApJ, 417, 220
Kenyon, S. J., Dobrzycka, D., & Hartmann, L. 1994, AJ, 108, 1872
Liseau, R., & Sandell, G. 1986, ApJ, 304, 459
Looney, L. W., Mundy, L. G., & Welch, W. J. 1997, ApJ, 484, L157
Lubow, S. H., & Ogilvie, G. I. 2000, ApJ, 538, 326
Mathieu, R. D. 1994, ARA&A, 32, 465
Melo, C. H. F., Covino, E., Alcalá, J. M., & Torres, G. 2001, A&A, 378, 898
Momose, M., Ohashi, N., Kawabe, R., Nakano, T., & Hayashi, M. 1998, ApJ, 504, 314
Ochi, Y., Sugimoto, K., & Hanawa, T. 2005, ApJ, 623, 922
Pichardo, B., Sparke, L. S., & Aguilar, L. A. 2005, MNRAS, 359, 521
Rodríguez, L. F., Curiel, S., Cantó, J., Loinard, L., Raga, A. C., & Torrelles, J. M. 2003a, ApJ, 583, 330
Rodríguez, L. F., Porras, A., Claussen, M. J., Curiel, S., Wilner, D. J., & Ho, P. T. P. 2003b, ApJ, 586, L137
Rodríguez, L. F., et al. 1998, Nature, 395, 355
Shang, H., Lizano, S., Glassgold, A., & Shu, F. 2004, ApJ, 612, L69
Shu, F. H., Adams, F. C., & Lizano, S. 1987, ARA&A, 25, 23
Shu, F., Najita, N., Ostriker, E., Wilkin, F., Ruden, S., & Lizano, S. 1994, ApJ, 429, 781
Smith, K. W., Bonnell, I. A., & Bate, M. R. 1997, MNRAS, 288, 1041
Snell, R. L., Loren, R. B., & Plambeck, R. L. 1980, ApJ, 239, L17
Stocke, J. T., Hartigan, P. M., Strom, S. E., Strom, K. M., Anderson, E. R., Hartmann, L. W., & Kenyon, S. J. 1988, ApJS, 68, 229
Strom, K. M., Strom, S. E., & Vrba, F. J. 1976, AJ, 81, 320
Takakuwa, S., et al. 2004, ApJ, 616, L15
Tohline, J. E. 2002, ARA&A, 40, 349